Journal of Marine Systems 241 (2024) 103916

Contents lists available at ScienceDirect

Journal of Marine Systems

journal homepage: www.elsevier.com/locate/jmarsys

Seasonality modulates particulate organic carbon dynamics in mid-latitudes of South Pacific and South Atlantic Oceans

Mariana B. Bif *, Jacqueline S. Long, Kenneth S. Johnson

Monterey Bay Aquarium Research Institute (MBARI), Moss Landing, CA, United States

ARTICLE INFO

Keywords:
Biological carbon pump
Marine carbon cycle
Particulate organic carbon
Primary production
Southern Ocean
Transfer efficiency

ABSTRACT

Here we used data from six BGC-floats deployed in the southeast Pacific and southwest Atlantic Oceans, within the Southern Ocean's Subtropical Zone, to assess the seasonality of particulate organic carbon production from phytoplankton (POC_{phyto}) and estimate POC transfer efficiencies at 100 m below the euphotic zone (T_100). While small particles <100 μM dominated the mixed layer, large particles >100 μM comprised a significant fraction of POC_{phyto} below the mixed layer in both areas, possibly due to a "shade flora" composed by large diatoms. POC_{phyto} was highly seasonal with highest biomass accumulation in the Atlantic side for both small and large particles. In the Pacific, the seasonal change in small particle production ΔPOC_{phyto} was ~66 mg m^{-2} versus ~54 mg m^{-2} from large particles. In the Atlantic, ΔPOC_{phyto} was ~852 mg m^{-2} for small particles versus ΔPOC_{phyto} ~ 262 mg m^{-2} for large particles. Monthly T_100s in the Pacific ranged from 76% to 92% with maximum efficiencies during the deepening of the mixed layer depth. In the Atlantic, T_100s ranged from 43% to 76% with two periods of high T_100s: the first coinciding with the decline of large particles from the "shade flora", and the second coinciding with the deepening of the mixed layer during elevated small particle production.

1. Introduction

Particulate organic carbon (POC) production within the sunlit portion of the open ocean varies in magnitude across regions, dependent on light availability and nutrients that fuel primary production (Buesseler and Boyd, 2009; Siegel et al., 2014; Li et al., 2018; Boyd et al., 2019; Fan et al., 2020). A small fraction of POC resists fragmentation and remineralization in the euphotic zone and is available for export (Baker et al., 2017; Cavan et al., 2017; Rembauville et al., 2017; Haëntjens et al., 2020). The POC fraction that survives remineralization at a deeper reference depth relative to the winter mixed layer or the euphotic zone (Ez) is defined as transfer efficiency (TE) (Henson et al., 2012; Buesseler et al., 2020). Changes in TEs are related to changes in particle size, molecular composition and respiration rates and can significantly impact atmospheric carbon dioxide concentrations (Kwon et al., 2009) by affecting the overall efficiency of the biological carbon pump (BCP), which can be determined by assessing the magnitude of POC fluxes exported out of the ocean's surface and its attenuation at reference depths. Ultimately, particle export is responsible of transferring about 5.7 Pg C yr^{-1} out of the Ez (Buesseler et al., 2020). Understanding the different processes that control the BCP efficiency, such as TE, and their variability over space and time is of undoubted importance since carbon sequestration by the ocean is considered a valuable ecosystem service (Jin et al., 2020).

TEs have been globally estimated but large areas of the ocean remain unexplored especially regarding seasonal variability, such as the mid-latitudes considered here (Henson et al., 2012; Buesseler et al., 2020; de Melo Viríssimo et al., 2022). A study conducted in the Northern Red Sea explored the relationships between TE and export efficiency in controlling the efficiency of the BCP (Kienast and Torfstein, 2022). For this assessment, the authors considered TE as the fraction of carbon surviving 100 m below the Ez in relation to POC at Ez, a term defined as T_100 (Buesseler and Boyd, 2009; Buesseler et al., 2020). The efficiency of the BCP was estimated as the product of T_100 and export efficiency, which was defined as the fraction of net primary production that leaves Ez [also defined as export ratio (Buesseler et al., 2020)]. While T_100s were lower during summer relative to winter (50% vs 95% respectively), export efficiencies were higher during summer than winter (40% vs 20% respectively) resulting in a similar BCP efficiency for both seasons around 20%.

* Corresponding author.
E-mail address: mariana@mbari.org (M.B. Bif).

https://doi.org/10.1016/j.jmarsys.2023.103916
Received 4 January 2023; Received in revised form 26 June 2023; Accepted 4 July 2023
Available online 8 July 2023

POC production and export can be observed and quantified using data collected by biogeochemical floats (BGC-floats) equipped with bio-optical sensors that measure backscattering at 700 nm (b_{bp}, a proxy for POC) and fluorescence (a proxy for chlorophyll-*a*, hereafter chl_fluor). A limitation of using BGC-floats to observe BCP processes is that most floats operate at 5–10 day cycles. A sampling frequency > 5 days is not enough to solve for sinking velocities (Briggs et al., 2020), which is the temporal term required to estimate particle fluxes and, ultimately, the efficiency of BCP (Giering et al., 2017; Buesseler et al., 2020; Kienast and Torfstein, 2022). Still, BGC-floats provide high spatiotemporal resolution of particle distributions and are proven suitable platforms to study the Southern Ocean where sampling is limited during wintertime (Rembauville et al., 2017; Uchida et al., 2019; Briggs et al., 2020). A method developed by Briggs et al. (2011) for underwater gliders separates b_{bp} and chl_fluor optical signals into large particles (>100 μm) and small particles (<100 μm). The method was further adapted to BGC-float data with global applicability enabling observations of seasonal POC production of different particle size fractions in the North Atlantic (Bol et al., 2018; Briggs et al., 2018; Briggs et al., 2020), the Southern Ocean (Briggs et al., 2020) and the Red Sea (Brewin et al., 2022).

Here we take advantage of data provided by BGC-floats deployed in two sectors of the Southern Ocean's Subtropical Zone (STZ) (Orsi et al., 1995; Gray et al., 2018), in the southeast Pacific Ocean (between 35 and 42°S, 97–109°W) and in the southwest Atlantic Ocean (between 27 and 39°S, 5–30°W) (Fig. 1), to characterize the vertical distribution of small and large particles within the Ez and assess the phytoplankton contribution to seasonal POC production (POC_{phyto}). We looked at particle Chl:C ratios to gather information about phytoplankton's seasonal ecophysiology such as photoacclimation and relief from nutrient limiting conditions (Parslow et al., 2001; Burt et al., 2018), since phytoplankton communities in those regions haven't been previously characterized. We then estimated monthly T_100 based on total POC.

2. Methods

2.1. Regional hydrography in the mid-latitudes of the Southeast Pacific and Southwest Atlantic oceans

Our study regions are located at similar latitudinal bands in the northernmost part of the Southern Ocean (Fig. 1) classified as the

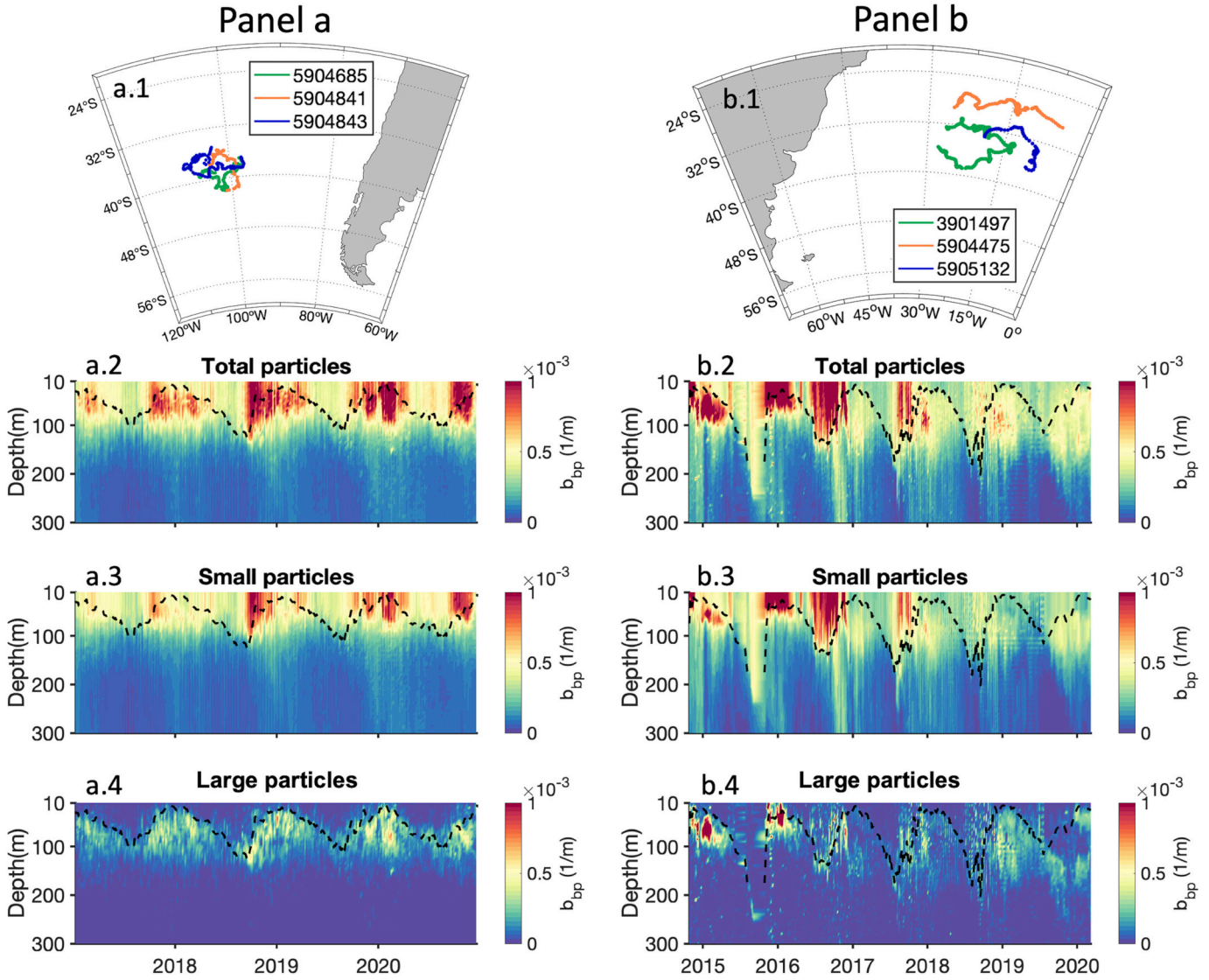

Fig. 1. Maps of the study areas encompassing the southeast Pacific (**a.1**) and the southwest Atlantic Oceans (**b.1**), showing the tracking for each float used in this study. Time-series of b_{bp} (1/m) distribution in the southeast Pacific and southwest Atlantic Oceans, showing total, small b_{bp} < 100 μm and large b_{bp} > 100 μm signals in the Pacific (**a.2-a.4**); and total, small b_{bp} < 100 μm and large b_{bp} > 100 μm signals in the Atlantic (**b.2-b.4**). Dashed lines indicate mixed layer depths (m), and January of each year is marked in the x-axis. Mean Ez is 172(±14) m in the Pacific and 157(±39) m in the Atlantic.

Subtropical Zone (STZ), which lies between Subtropical Gyres and the Subtropical Front across different basins (Orsi et al., 1995; Gray et al., 2018). For the timespan considered here, the Pacific region also received occasional contributions from cold and nutrient-enriched waters from the Subantarctic Front Zone [SAZ is defined as cooler and fresher than STZ (Gray et al., 2018); Fig.S1]. Here we treat both regions as belonging to the STZ. Relative to other zones, the STZ is characterized by warm temperatures, surface nitrate concentrations modestly above detection limit (Wyatt et al., 2014; Gray et al., 2018; Bif et al., 2022) (Fig.S2) and moderate NPP estimated around 4.6 Pg C y^{-1} between 30 and 40°S (Johnson and Bif, 2021), limited by iron and light availability (Klunder et al., 2011).

2.2. Float and satellite data acquisition

A total of six floats were used in this study (Fig. 1), three located in the southeast Pacific Ocean (WMO I.Ds. 5904685, 5904841 and 5904843) and three in the southwest Atlantic Ocean (WMO I.Ds. 3901497, 5904475 and 5905132). Quality-controlled float profile data in Argo Sprof files for salinity, temperature, nitrate (when available) and bio-optics were downloaded from the Global Data Assembly Center (Argo, 2023). Only data flagged "good" (except for b_{bp} data, which is not quality-controlled) were used for the analyses. Data for the Pacific sector between Sep-2017 to Dec-2020 was collected by three APEX floats deployed by the SOCCOM program. Data for the Atlantic sector between Oct-2014 and Mar-2020 were collected by a Provor III float (3901497, UK-Bioargo program), a NAVIS float (5904475, SOCCOM program) and an APEX float (5905132, SOCCOM program). To verify which Southern Ocean zones the floats were sampling, we performed an analysis based on definitions from Orsi et al. (1995) and Gray et al. (2018) and considered STZ as the zone where $\theta_{100m} > 11$ °C and $[NO_3^-]$ is detectable. SAZ has $\theta_{400m} > 5$ °C (Figs.S1, S2).

For nitrate measurements, floats were equipped either with Submersible Ultraviolet Nitrate Analyzer (SUNA) or In Situ Ultraviolet Spectrophotometer (ISUS). Details on data quality-control applied for this sensor can be found at Johnson et al. (2017) and Maurer et al. (2021). For bio-optics measurements, floats were equipped with Seabird-Wetlabs sensors that measured chl_fluor (fluorometer, 470 nm of excitation and 695 nm of emission) and b_{bp} at 700 nm. Details on sensor performance and reliability by comparing with satellite and ship data have been previously published (Sullivan et al., 2013; Haëntjens et al., 2017; Johnson et al., 2017; Roesler et al., 2017). All floats profiled every ~10 days from the surface down to 2000 m except for #3901497, that profiled down to 1000 m every ~5 days.

The ratio of fluorescence to chlorophyll is known to vary over time and space scales such as those occupied by the floats (Roesler et al., 2017; Long et al., 2021). Roesler et al. (2017) recommend a global mean adjustment of the factory calibration by dividing computed chlorophyll by 2. However, there are significant regional variations in this correction factor. To adjust for this variability through time and space, 8-day averaged MODIS-Aqua 0.17° resolution data were downloaded for [chl] (GSM; Maritorena et al., 2002). Satellite [chl] estimates were matched to adjusted float chlorophyll [chl_fluor] profile locations within the satellite pixel area, and nearest in time. A gain adjustment between the satellite data and float data (averaged within the 1st optical depth) was applied point by point for each profile, through depth, to adjust float chlorophyll fluorescence to a value consistent with the global remote sensing data (Fig.S3). Missing satellite data due to cloud cover or high sun glint were linearly interpolated (interp1 function, Matlab®). Satellite data were downloaded from http://sites.science.oregonstate.edu/ocean.productivity/index.php.

2.3. b_{bp} and chl_fluor data processing

For b_{bp} data, we first performed a visual quality-control to remove profiles containing spikes >0.04 1/m (which is near the instrument saturation value) and drifts. Raw data was then separated into small (<100 μm) and large (>100 μm) particles by using a modified version from Briggs et al. (2020), greatly detailed in their supplementary material. The limit of detection for small particles defined here is predicted to fall within 0.2–0.5 μm of particle size-range according to assessments using b_{bp} at 526 nm and b_{bp} at 532 nm (Dall'Olmo et al., 2009; Organelli et al., 2018). The partitioning between small and large particles was originally developed for the North Atlantic and higher latitudes of the Southern Ocean. Because our study region did not have considerable spike frequencies that are attributed to high flux of biomass found in those areas, we applied a 40-point minimum and maximum filters instead of 11-point to separate large particles from small particles plus the sensor background noise. Another modification was the instrument noise estimate, now calculated for each float using winter profiles only. When possible, the noise was estimated per year per float using the previous winter data and then propagated over a year. In years when a float did not start sampling in the wintertime, the instrument background estimated from the following year was considered and retroactively applied. These values averaged $3.6 \times 10^{-4} \pm 1.4 \times 10^{-4}$ 1/m in the South Atlantic and $2.5 \times 10^{-4} \pm 2.6 \times 10^{-5}$ 1/m in the South Pacific, about an order of magnitude lower than b_{bp} POC signals.

For chl_fluor, the adjusted data (provided from the Argo snapshot corrected for NPQ (Xing et al., 2012) and an in situ dark offset) were further corrected using the satellite gain adjustment (Fig.S3) described in the previous section. Total chl_fluor was then separated into concentrations belonging to small and large particles following the same method as for b_{bp} (Briggs et al., 2020).

The placement of large and small b_{bp} particles in the upper ocean was vertically heterogeneous with clear differences above and below the mixed layer (ML) in both study areas. In order to better characterize particle accumulation in those two distinct layers, we divided the upper ocean in two sections, (1) the region within the mixed layer depth, hereafter 0-MLD and (2) between the bottom of the MLD and the median Ez of each region, hereafter MLD-Ez (Ez calculation is explained in the next section). We then compiled our dataset and used the mean monthly binned data to estimate the climatology of b_{bp} accumulation of small and large particles in each layer. The climatology dataset can be found in the supplementary material of this manuscript. In order to estimate phytoplankton carbon accumulation (Graff et al., 2015; Arteaga et al., 2022):

$$b_{bp470}\ (1/\mathrm{m}) = (470/700)^{-1} \tag{1}$$

$$POC_{phyto}\ \left(\mathrm{mg/m^3}\right) = 12,128 \times b_{bp470} + 0.59 \tag{2}$$

In order to estimate TE, we converted b_{bp700} to total POC (Johnson et al., 2017) as:

$$POC\ \left(\mathrm{mg/m^3}\right) = 31,200 \times b_{bp} + 3.04 \tag{3}$$

Our data is shown as a climatological mean of POC volumetric concentrations (mg/m^3) and POC stocks (mg/m^2). Stocks were estimated for each month of the climatology using trapezoidal integration (trapz function, Matlab®).

2.4. Ez, MLD, export ratio, and T_100

We estimated Ezs of each basin assuming they comprise the primary production zone, defined as the depth at which chlorophyll is 10% of maxima value and close to 0.1% PAR (Maiti et al., 2010; Marra et al., 2014; Owens et al., 2015; Buesseler et al.,2020):

$$Ez\ (\mathrm{m}) = Z \text{ of } 0.1^{*}\ chl\_fluorMax\ below\ Z_{chl\_fluorMax} \tag{4}$$

where chl_fluorMax is the depth of maxima [chl_fluor] for each profile. We then estimated the median Ez using summer profiles (June, July and August) for each basin since most particle production happens during those months, and use this absolute value for subsequent calculations. MLDs were calculated assuming a density threshold of 0.03 kg

m^{-3} (de Boyer Montégut et al., 2004). Mean monthly T_100s for each basin were calculated using total POC data following Buesseler et al. (2020). We assume.

$$T\_100\ (\%) = POC_{\text{medianEz+100m}}/POC_{\text{medianEz}}{}^{*}\ 100 \quad (5)$$

Where $POC_{medianEz}$ is the mean monthly POC concentration at Ez and $POC_{medianEz+100m}$ is the mean monthly POC concentration at 100 m below Ez. We then computed the absolute mean T_100 for each basin using monthly T_100s. The variability of monthly T_100s around the absolute mean T_100 and the amplitude of this variability are discussed further.

2.5. Statistics

In order to determine the seasonal variability of particle production within ocean layers (i.e., 0-MLD and MLD-Ez) and better characterize seasonal particle accumulation at each basin, we applied a multi-step statistical process. For each float profile, we estimated mean b_{bp} at each layer and then divided all data into seasons: spring (September, October and November), summer (December, January and February), fall (March, April and May) and winter (June, July and August). We then built frequency histograms for each dataset fixed by a linear x-axis based on min and max b_{bp} values of the whole dataset at 20 bins of resolution (Small b_{bp} accumulation in the Atlantic during spring, for example; Fig. S4-S7).

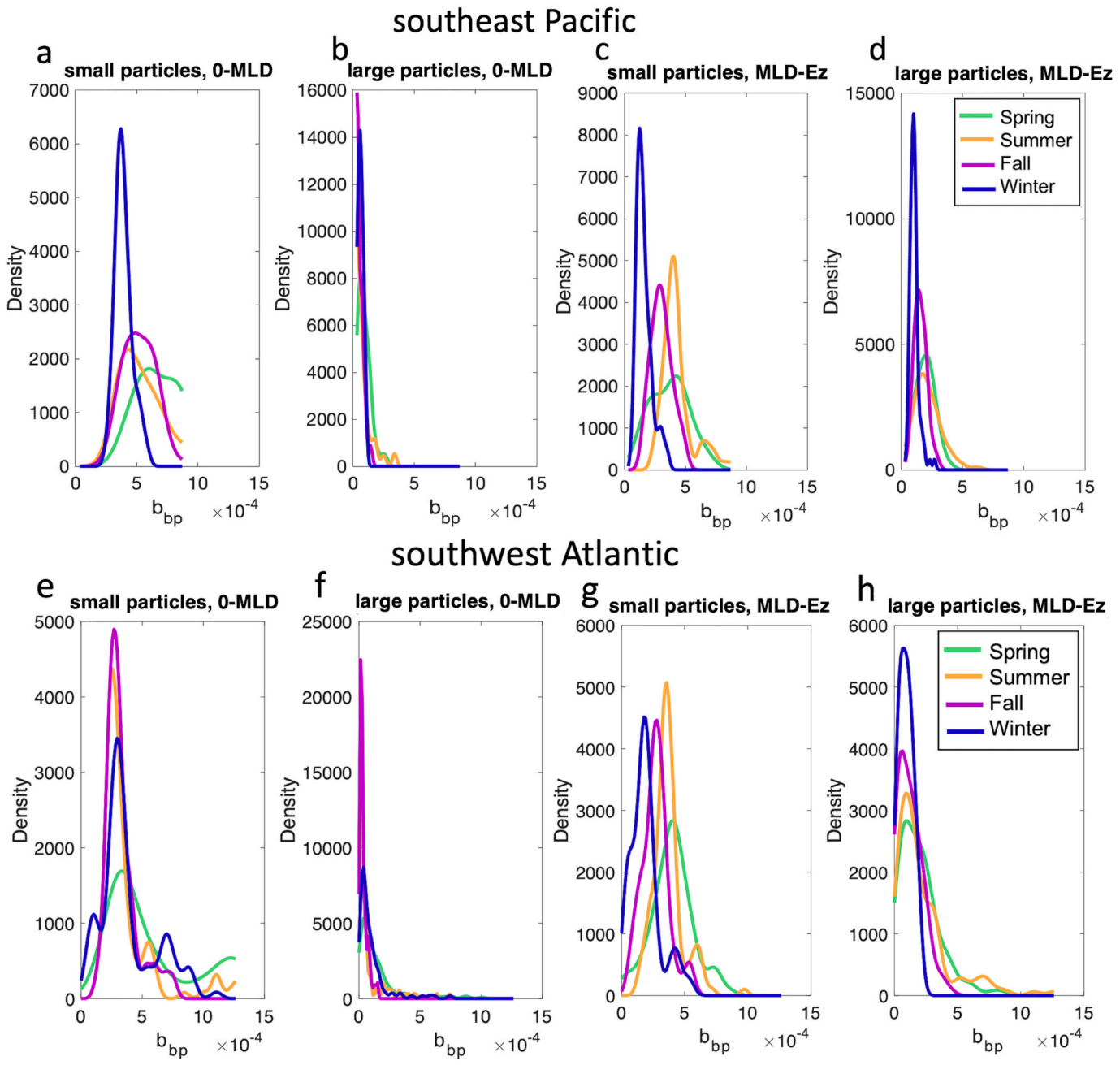

Fig. 2. Kernel density plots of mean seasonal b_{bp} accumulation in the southeast Pacific (**a-d**) and southwest Atlantic (**e-h**) oceans. Superimposed plots were originally extracted from Figs.S4-S7. Different seasons overlap for each particle size, depth range, and ocean region. Colored lines indicate each season, e.g., green: spring (September–November); orange: summer (December–February); purple: fall (March–May); blue: winter (June–August). (For interpretation of the references to colour in this figure legend, the reader is referred to the web version of this article.)

Since b_{bp} data is not normally-distributed, we fit the non-parametric Kernel density distribution (Szabó et al., 2021) to each histogram (fitdist function with normal smoothness mode, Matlab® Statistics and Machine Learning Toolbox). The Kernel distribution showed a unique shape for each season, large (small) particles and layers, like a fingerprint reflecting b_{bp} accumulation within each data subset (Fig.S4-S7). The agreement between Kernel and data distributions are illustrated by quantile-quantile (Q-Q plots) for each dataset. All plots are close to a linear relationship, meaning this is a statistically-robust approach to explain b_{bp} seasonal distribution (Thode, 2002). We then compared the Kernel plot areas among each group and computed *p*-values using the Kruskal-Wallis test (kruskalwallis function, Matlab® Statistics and Machine Learning Toolbox) assuming 5% of significance level (Table S3), where $p < 0.05$ assumes that particle accumulation was not similar during the two corresponding seasons.

3. Results and discussion

3.1. Seasonal accumulation of particles above the Ez

Particle production in the Pacific region was dominated by small particles that were concentrated mainly above the ML, while large particles were concentrated between the bottom of the ML and the Ez (172 ± 14 m) following the base of the ML over the year (Fig. 1 panel a). The accumulation's magnitude varied within seasons and was dependent on particle size (large vs small) and vertical placement (0-MLD vs MLD-Ez). Table S3 contains p-values from the Kruskal-Wallis multi-comparison analysis between the Kernel plots (Fig. 2) for each season, particle size and vertical placement. In the surface layer between 0-MLD, the magnitude of small particle accumulation was statistically similar during spring, summer and fall ($p > 0.05$) but with a stronger correlation between spring and summer ($p = 0.3$), and was at minimum during winter ($p < 0.05$) (Fig. 2a). Accumulation between MLD-Ez was also observed at those same seasons (Fig. 2c). During spring and summer, large particles accumulated between 0-MLD at similar magnitude ($p = 0.916$) (Fig. 2b), while most accumulation happened between MLD-Ez but at different magnitudes ($p < 0.05$) (Fig. 2d).

In the Atlantic region, particle accumulation also showed vertical heterogeneity (Fig. 1 panel b) with small particles dominating the 0-MLD layer and being mainly responsible for the backscatter signal below the Ez (157 ± 39 m). Large particles were concentrated between MLD-Ez but with a patchier distribution in comparison to the Pacific. Between 0-MLD, small particles accumulated at similar magnitudes during winter and spring (Fig. 2e), and at a lower magnitude during summer and fall with relatively weak correlation to the threshold of $p < 0.05$ ($p = 0.063$). In the MLD-Ez layer, accumulation of small particles was similarly high during spring and summer and similarly low during winter and fall (Fig. 2g), indicating a seasonal shift in particle accumulation toward warmer months in comparison to 0-MLD, when particles accumulated mainly during winter and spring. Large particles had low accumulation during all seasons, with a weak correlation between summer and winter ($p = 0.068$) (Fig. 2f). Accumulation of large particles between MLD-Ez was increased in relation to the upper layer for all seasons, with spring and summer showing similarly high accumulation ($p = 0.117$) (Fig. 2h).

The heterogeneous vertical distribution of particles above the Ez has been documented for high-nutrient low-chlorophyll areas of the Southern Ocean and reflects the varying life-strategies of different phytoplankton groups. High concentrations of large particles below the ML are often referred to as "shade flora", a feature mainly composed by large diatom species (Sournia, 1982; Kemp et al., 2006; Queguiner, 2013; Kemp and Villareal, 2018). Their placement in the subsurface is the result of a physiological response to nutrient availability in the euphotic zone. Low surface iron and/or silicate conditions during warm seasons promote an increase in sinking rates of large diatoms that end up accumulating in the subsurface, closer to the nutricline. Subsequent nutrient alleviation produces the opposite effect (Parslow et al., 2001; Gomi et al., 2010). In the Interpolar Frontal Zone, which Parslow et al. (2001) define as the zone between the northern and southern Polar Fronts (the northern front was defined as <2 °C near 200 m following Botnikov (1963) while the southern front was defined as the deepening of the minimum temperature layer northward following Gordon (1971)), these large cells form the subsurface chlorophyll maxima near the ML. The feature is found at depths as shallow as 60 m in the summer to >100 m in the spring when the ML is deeper.

In the region off the Kerguelen Plateau, located in the Indian sector of the Southern Ocean, high-biomass assemblages of large diatoms form permanent features below the ML at depths >100 m with a stable dominance of *Fragilariopsis pseudonana* and *F. kerguelensis* chains (Armand et al., 2008). Despite being found at lower densities in comparison to small phytoplankton groups, these large cells have great potential for carbon export (Kemp et al., 2006; Grigorov et al., 2014). Similar to previous studies that observed a "shade flora" in other regions of the Southern Ocean, both of our study regions showed a permanent subsurface feature composed of large particles that followed the base of the ML (Fig. 1), with increased accumulation during spring and summer.

3.2. Seasonal POC_{phyto} accumulation and Chl:C ratios

In order to observe seasonal phytoplankton accumulation with insights on the ecophysiology, we estimated the climatology of POC_{phyto} and Chl:C ratios (Fig. 3). In the southeast Pacific Ocean, the deepening of the ML during fall coincides with an increase of Chl:C on both small and large particles, first happening in the layer between MLD-Ez and later above the ML (Fig. 3a,b). Two mechanisms have been identified as responsible for shifts in the ratios: nutrient relief and photoacclimation (Parslow et al., 2001; Burt et al., 2018). This feature is formed at the end of the productive season when the ML layer is still relatively shallow (<50 m) and is timed with the displacement of particles below the ML to deeper waters, possibly getting closer to the ferrocline earlier than surface cells, so a more plausible explanation for the ratio increase is nutrient relief. Indeed, phytoplankton increase Chl:C ratios under excess-nitrate low-iron conditions (Schrader et al., 2011; Burt et al., 2018). These high ratios are then maintained within the ML during wintertime when light is increasingly limited, possibly having a photoacclimation component. The high productive season during spring and summer is marked by decreasing Chl:C ratios, signaling nutrient limitation and/or alleviation from light limitation.

The seasonal change in the integrated small particles stock in the Pacific was $\Delta POC_{phyto} \sim 66$ mg m^{-2} (October POC_{phyto} – July POC_{phyto}), modestly higher than large particles as $\Delta POC_{phyto} \sim 54$ mg m^{-2} (February POC_{phyto} – August POC_{phyto}) (Fig. 3a,b). However, the background concentration of small particles was much higher: ~123 mg m^{-2} in July, when small particles were at the lowest versus large particles minimum of ~23 mg m^{-2} in August. Small particle concentrations peaked at 216 mg C m^{-2} in October, while maximum POC_{phyto} concentration of large particles was 76 mg C m^{-2} in February, about a third of the small particles' concentration. A portion of b_{bp} signals, especially in the small particle fraction, is attributed to detritus and non-algal particles (b_{bp}^{k}) that has proven challenging to estimate as it produces high uncertainties of over one order of magnitude from the mean for an ocean region (Bellacicco et al., 2019, supplementary material Tables S3, S4). Although we employ a method that converts b_{bp} into POC_{phyto} to remove the effect of non-phytoplankton particles, our approach does not remove those seasonal changes in b_{bp}^{k}. Background backscatter tends to decrease Chl:C in the STZs during warmer months (Bellacicco et al., 2019) and might underestimate the peaks in Chl:C that we observe during spring and summer.

In the southwest Atlantic, different mechanisms appear to drive POC_{phyto} accumulation and Chl:C ratios in the two layers when compared to mechanisms in the Pacific. The Chl:C ratio trends of the small particle fraction in the mixed layer are inversed from trends in

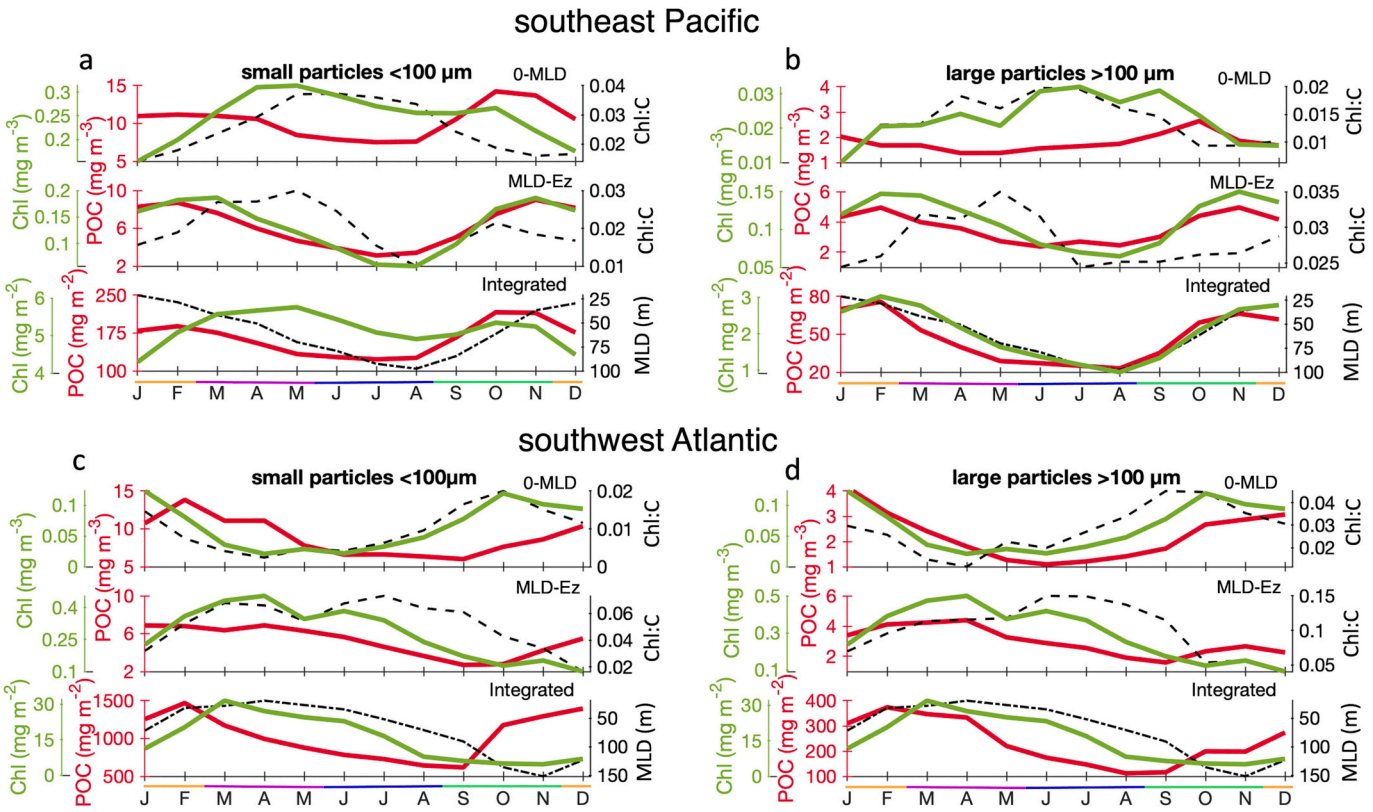

Fig. 3. Temporal variability of POC_{phyto} (red lines), Chl (green lines), Chl:C ratios (black homogeneous dashed lines) and MLDs (black heterogeneous dashed line). Data is shown for small and large particles in the southeast Pacific (**a-b**) and southwest Atlantic Oceans (**c-d**). Data is subdivided in three sub-panels. First panels represent mean monthly values within the ML; second panels represent mean monthly values between the ML and median Ez; third panels represent integrated mean monthly stocks between surface and median Ez. Data for $b_{bp} \pm 1$ standard deviation used for the POC_{phyto} calculations are reported in Tables S1 and S2. Colored lines along the x-axis indicate seasons: spring (purple), summer (blue), fall (green) and winter (orange). (For interpretation of the references to colour in this figure legend, the reader is referred to the web version of this article.)

ratios observed in the Pacific (Fig. 3a and c). In part, this is due to the MLD maxima occurring at different times; November in the Atlantic and August in the Pacific. Chl:C increases within the ML as it deepens by end of the winter (Fig. 3c,d), a process that is similar to the Pacific region but during fall. The opposite happens in the layer between MLD-Ez where high ratios are maintained during fall and wintertime coinciding with [chl_fluor] that are 4 to 5 times higher than the upper layer. Biomass between MLD-Ez is also elevated in those months, but a deep-biomass feature is only observed in the large particles fraction. The high Chl:C between MLD-Ez could be related to photoacclimation rather than nutrient alleviation since it is inverse to the deepening of the ML, although low light combined with elevated nutrients also result in high Chl:C (Graff et al., 2016).

Perhaps the most interesting feature found below the ML is the Chl:C that is an order of magnitude higher than everywhere else. This could indicate a unique phytoplankton assemblage and may contradict the idea that the subsurface is composed by microbial communities of similar composition to the upper layer (Parslow et al., 2001; Armand et al., 2008). Previous studies on "shade flora" identified phytoplankton groups and their respective Chl:C in the Southern Ocean, but were carried at higher latitudes than the STZ such as the Interpolar Frontal Zone and South of the Polar Front. In those high-latitude regions, low Chl:C large-celled phytoplankton assemblages have been recorded such as *Dactyliosolen, Asteromphalus, Membraneis, Thalassiosira* in 2002 and 2003. Their low Chl:C ratios were related to species physiology, low nutrient and temperature, and high light intensities (Gomi et al., 2010) – opposite environmental conditions than observed in our study. Interannual variability in the community composition have also been recorded, and 1998 communities in those high latitudes were composed by *Pseudo-nitzchia, Thalassiothrix, Chaetoceros and Proboscia* (Kopczynska et al., 2001). Adding to the previous studies, our results indicate that the "shade flora" assemblages are not only variable through the years and at the different Southern Ocean Zones, but vary through seasons and can be different from communities found within the ML.

In terms of POC_{phyto} accumulation, the Atlantic region had significantly higher magnitudes of biomass than the Pacific (Fig. 3c,d). The concentration of small particles peaked in February at 1470 mg C m^{-2}, almost 7 times higher than in the Pacific. Large particles corresponded to a maxima of 374 mg C m^{-2} in February, about a quarter of the magnitude of small particles and 5 times higher than the Pacific. Total accumulation was $\Delta POC_{phyto} \sim 852$ mg m^{-2} for small particles (February–September) versus $\Delta POC_{phyto} \sim 262$ mg m^{-2} (February–August) for big particles. These differences may be explained by higher atmospheric iron deposition rates in the Atlantic stimulating productivity (Klunder et al., 2011; Myriokefalitakis et al., 2018).

Large phytoplankton cells in the Interpolar Front Zone were responsible for 20–50% of total POC_{phyto} accumulation in the water column, with the highest contributions during warmer months (Parslow et al., 2001). In our two study regions, these large particles contributed to about 45% in the Atlantic and 25% in the Pacific. Thus, in addition to ΔPOC_{phyto} accumulating at different magnitudes among the two STZs, different particle sizes contribute at different proportions to the overall accumulation of POC_{phyto} but within the same range as in the Interpolar Front Zone. Considering that sampling methods to collect phytoplankton cells during research cruises often do not capture deeper communities (Queguiner, 2013), and that remote sensing cannot reach deeper water layers, the use of biogeochemical floats equipped with backscatter sensors significantly contributes to a more complete observation of

phytoplankton vertical distribution including the "shade flora", and to a more complete estimate of POC_{phyto} seasonal accumulation.

3.3. T_100

T_100s have been estimated for an array of environments using sediment-traps and thorium-234 data, given a single value per ocean region (Buesseler et al., 2020), but the southeast Pacific and southwest Atlantic haven't been assessed. $T = 100\%$ indicates some degree of POC attenuation below Ez, and consequently a decrease in the likelihood that sinking POC will be sequestered to depths far from the air-sea interaction layer. Global observations could not find an apparent relationship between T_100, the magnitude of carbon accumulation or Ez depths, other than T_100s appear to be higher with deeper Ezs (>100 m) (Buesseler et al., 2020). The Southern Ocean STZs considered in our study fall into this category with median Ezs >150 m, and although located at similar latitudinal bands, magnitudes of POC_{phyto} accumulation and T_100s are remarkably different between regions (Fig. 4).

Using the T_100 metric, we estimated the climatologies for the Pacific and Atlantic regions as monthly T_100s. In the Pacific, the absolute mean T_100 was higher than the Atlantic (85% versus 61%, respectively) and the amplitude of monthly T_100's around the absolute mean were lower (Fig. 4; Table 1). In the Pacific, a minimum T_100 of 76% was observed in October, representing a 10.6% decrease from the absolute mean. A maximum of 92% was observed in May, representing a 8.2% increase from the absolute mean. The highest monthly T_100s happened during fall and winter when small and large POC_{phyto} declined, also coinciding with deep MLDs (Fig. 3a,b). In this scenario, the deepening of the ML could have favored particle export at the end of the productive season, a process defined as the mixed layer pump (Dall'Olmo et al., 2016; Boyd et al., 2019; Lacour et al., 2019).

In the Atlantic, two monthly T_100 increasing trends were observed: the first increase happened during fall and peaked at 76% in June, representing a 24.6% increase in relation to the absolute mean (Fig. 4, Table 1). Elevated T_100s coincided with the decline of POC_{phyto} in the MLD-Ez layer especially for the large particles (Fig. 3c,d). Gravitational sinking of large particles here could have been the major driver of particle export (Buesseler et al., 2007; Kwon et al., 2009; Boyd et al., 2019). In this case, big particles composing the "shade flora" could have been an important fraction of the exported POC out of the Ez. A rapid T_100 decline is then observed with a minimum of 43% in August, 29.5% lower than the absolute mean. A second positive T_100 trend is observed during spring with a maximum of 75% in November, or a 23.0% increase in relation to the absolute mean. This second T_100 maximum coincided with deep MLDs and elevated POC_{phyto} in the small particle fraction. In this scenario, the deep ML could have favored small particles to sink during the productive season.

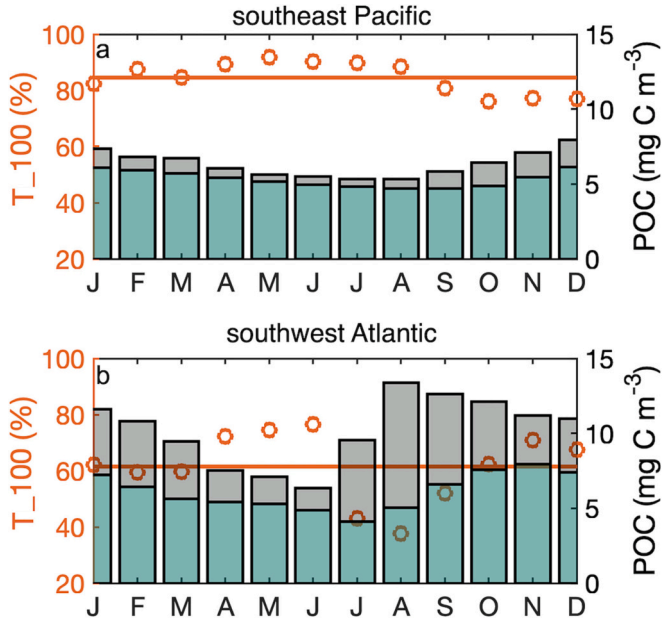

Fig. 4. Temporal variability of T_100 ratios in the southeast Pacific (**a**) and southwest Atlantic oceans (**b**). Orange dots represent mean T_100 for each calendar month, with the absolute mean represented by the continuous orange line. Bar graphs represent mean monthly POC concentrations (mg C m^{-3}) at median Ez (green + gray shaded area) and median Ez_{+100} (green shaded area). (For interpretation of the references to colour in this figure legend, the reader is referred to the web version of this article.)

Table 1
Mean monthly transfer efficiencies out of Ez (T_100) in the southeast Pacific and southwest Atlantic Oceans extracted from Fig. 4 and deviations from the absolute climatological means for each basin.

		Southeast Pacific		Southwest Atlantic	
Season	Month	Monthly T_100	Variability around absolute mean T_100 (85%)	Monthly T_100	Variability around absolute mean T_100 (61%)
	Sept	81%	−4%	52%	−9%
Spring	Oct	76%	−9%	62%	1%
	Nov	77%	−8%	71%	10%
	Dec	77%	−8%	67%	6%
Summer	Jan	82%	−3%	62%	1%
	Feb	88%	3%	59%	−2%
	Mar	85%	0%	60%	−1%
Fall	Apr	89%	4%	72%	11%
	May	92%	7%	74%	13%
	Jun	90%	5%	76%	15%
Winter	Jul	90%	5%	43%	−18%
	Aug	88%	3%	38%	−23%

One limitation of using BGC-float data to estimate BCP metrics is that most floats, such as those used here, have a sampling temporal resolution between 5 and 10 d intervals and vertical resolution of ≥10 m in the mesopelagic. Such resolution does not allow for tracking particle sinking speeds and, consequently, estimate POC fluxes. According to Briggs et al. (2020), "typical sinking velocities (50-100 m d^{-1}) require temporal frequencies of <5 d in order to sample a sinking pulse multiple times in the upper mesopelagic, where concentrations are more likely to be high enough to constrain sinking velocity measurements." In this study we could have applied constant sinking rates found in the literature for small and large particles, and then make a rough estimate of POC fluxes. However, since seasonal changes in the local microbial community composition were likely driving POC production, sinking rates would vary through seasons. Assuming a general sinking velocity for each size fraction would be a misrepresentation of the system and would introduce an artifact when estimating vertical attenuation rates.

4. Concluding remarks

The Southern Ocean STZ is a dynamic environment where significant POC_{phyto} accumulation happens during spring and summer months. When contrasting the southeast Pacific with the southwest Atlantic STZs, POC_{phyto} accumulation was driven by both small and large particles but was higher in magnitude in the Atlantic region. Although we could not access phytoplankton community composition, our results point toward a permanent "shade flora" as a subsurface chlorophyll and POC feature between MLD-Ez in both regions, likely composed by large diatoms. In the Pacific, elevated transfer efficiencies after the productive season were likely facilitated by the mixed layer pump. In the Atlantic, high T_100s were first driven by large particles from the "shade flora", and later by small particles sinking during high production, facilitated by the mixed layer pump. The persistently high subsurface Chl:C signature from the "shade flora" suggests a unique phytoplankton

assemblage that is different from the surface and an important fraction of POC_{phyto} production and export. The ability to characterize this subsurface layer that has been historically limited by observations as well as estimate monthly POC transfer efficiencies was facilitated by the high spatiotemporal sampling resolution of BGC-floats deployed in the STZs.

CRediT authorship contribution statement

Mariana B. Bif: Conceptualization, Methodology, Formal analysis, Investigation, Data curation, Validation, Writing – original draft, Visualization. **Jacqueline S. Long:** Methodology, Validation, Formal analysis, Data curation, Writing – review & editing. **Kenneth S. Johnson:** Conceptualization, Resources, Visualization, Supervision, Writing – review & editing.

Declaration of Competing Interest

The authors declare the following financial interests/personal relationships which may be considered as potential competing interests:

Mariana Bernardi Bif reports financial support was provided by National Science Foundation. Kenneth Johnson reports financial support was provided by National Science Foundation.

Data availability

Quality controlled BGC-float data was downloaded from Argo GDAC: https://www.seanoe.org/data/00311/42182/ (2021–01 snapshot, key 80,076). Processed bbp data used in this study can be found in the supplementary material. Chlorophyll data from satellite can be accessed from (June 2021): http://sites.science.oregonstate.edu/ocean.productivity/index.php. Processed bbp climatology data is found in this article's supplementary material

Acknowledgements

The authors would like to thank all the personnel involved in efforts to build, deploy floats and process data. We also thank UK BioArgo - BODC project to make data available for the float WMO#3901497, and the SOCCOM project for data availability of the remaining floats. All authors were supported through MBARI by the David and Lucile Packard Foundation. This work was sponsored by Southern Ocean Carbon and Climate Observations and Modeling (SOCCOM) Project under the NSF Awards PLR-1425989 and OPP-1936222, with additional support from NOAA and NASA. Logistical support for this project in the Antarctic was provided by the U.S. National Science Foundation through the U.S. Antarctic Program.

Appendix A. Supplementary data

Supplementary data to this article can be found online at https://doi.org/10.1016/j.jmarsys.2023.103916.

References

Argo, 2023. Argo Float Data and Metadata from Global Data Assembly Centre (Argo GDAC). SEANOE. https://doi.org/10.17882/42182.

Armand, L.K., Cornet-Barthaux, V., Mosseri, J., Queguiner, B., 2008. Late summer diatom biomass and community structure on and around the naturally iron-fertilised Kerguelen plateau in the Southern Ocean. Deep-Sea Res. II Top. Stud. Oceanogr. 55 (5–7), 653–676.

Arteaga, L.A., Behrenfeld, M.J., Boss, E., Westberry, T.K., 2022. Vertical structure in phytoplankton growth and productivity inferred from biogeochemical-argo floats and the carbon-based productivity model. Glob. Biogeochem. Cycles 36 (8) p. e2022GB007389.

Baker, C.A., Henson, S.A., Cavan, E.L., Giering, S.L., Yool, A., Gehlen, M., Belcher, A., Riley, J.S., Smith, H.E., Sanders, R., 2017. Slow-sinking particulate organic carbon in the Atlantic Ocean: magnitude, flux, and potential controls. Glob. Biogeochem. Cycles 31 (7), 1051–1065.

Bellacicco, M., Cornec, M., Organelli, E., Brewin, R.J.W., Neukermans, G., Volpe, G., Barbieux, M., Poteau, A., Schmechtig, C., d'Ortenzio, F., Marullo, S., 2019. Global variability of optical backscattering by non-algal particles from a biogeochemical-Argo data set. Geophys. Res. Lett. 46 (16), 9767–9776.

Bif, M.B., Bourbonnais, A., Hansell, D.A., Granger, J., Westbrook, H., Altabet, M.A., 2022. Controls on surface distributions of dissolved organic carbon and nitrogen in the Southeast Pacific Ocean. Mar. Chem. 104136.

Bol, R., Henson, S.A., Rumyantseva, A., Briggs, N., 2018. High-frequency variability of small-particle carbon export flux in the Northeast Atlantic. Glob. Biogeochem. Cycles 32 (12), 1803–1814.

Botnikov, V.N., 1963. Geographical position of the Antarctic convergence zone in the Antarctic Ocean. Soviet Antarctic Exped. Inform. Bull. 41, 324–327.

Boyd, P.W., Claustre, H., Levy, M., Siegel, D.A., Weber, T., 2019. Multi-faceted particle pumps drive carbon sequestration in the ocean. Nature 568 (7752), 327–335.

Brewin, R.J., Dall'Olmo, G., Gittings, J., Sun, X., Lange, P.K., Raitsos, D.E., Bouman, H. A., Hoteit, I., Aiken, J., Sathyendranath, S., 2022. A conceptual approach to partitioning a vertical profile of phytoplankton biomass into contributions from two communities. J. Geophys. Res. Oceans 127 p.e2021JC018195.

Briggs, N., Perry, M.J., Cetinić, I., Lee, C., D'Asaro, E., Gray, A.M., Rehm, E., 2011. High-resolution observations of aggregate flux during a sub-polar North Atlantic spring bloom. Deep-Sea Res. I Oceanogr. Res. Pap. 58 (10), 1031–1039.

Briggs, N., Guðmundsson, K., Cetinić, I., D'Asaro, E., Rehm, E., Lee, C., Perry, M.J., 2018. A multi-method autonomous assessment of primary productivity and export efficiency in the springtime North Atlantic. Biogeosciences 15 (14), 4515–4532.

Briggs, N., Dall'Olmo, G., Claustre, H., 2020. Major role of particle fragmentation in regulating biological sequestration of CO2 by the oceans. Science 367 (6479), 791–793.

Buesseler, K.O., Boyd, P.W., 2009. Shedding light on processes that control particle export and flux attenuation in the twilight zone of the open ocean. Limnol. Oceanogr. 54 (4), 1210–1232.

Buesseler, K.O., Lamborg, C.H., Boyd, P.W., Lam, P.J., Trull, T.W., Bidigare, R.R., Bishop, J.K., Casciotti, K.L., Dehairs, F., Elskens, M., Honda, M., 2007. Revisiting carbon flux through the ocean's twilight zone. Science 316 (5824), 567–570.

Buesseler, K.O., Boyd, P.W., Black, E.E., Siegel, D.A., 2020. Metrics that matter for assessing the ocean biological carbon pump. Proc. Natl. Acad. Sci. 117 (18), 9679–9687.

Burt, W.J., Westberry, T.K., Behrenfeld, M.J., Zeng, C., Izett, R.W., Tortell, P.D., 2018. Carbon: chlorophyll ratios and net primary productivity of subarctic Pacific surface waters derived from autonomous shipboard sensors. Glob. Biogeochem. Cycles 32 (2), 267–288.

Cavan, E.L., Henson, S.A., Belcher, A., Sanders, R., 2017. Role of zooplankton in determining the efficiency of the biological carbon pump. Biogeosciences 14 (1), 177–186.

Dall'Olmo, G., Westberry, T.K., Behrenfeld, M.J., Boss, E., Slade, W.H., 2009. Significant contribution of large particles to optical backscattering in the open ocean. Biogeosciences 6 (6), 947–967.

Dall'Olmo, G., Dingle, J., Polimene, L., Brewin, R.J.W., Claustre, H., 2016. Substantial energy input to the mesopelagic ecosystem from the seasonal mixed-layer pump. Nat. Geosci. 9, 820–823.

de Boyer Montégut, C., Madec, G., Fischer, A.S., Lazar, L., Iudicone, D., 2004. Mixed layer depth over the global ocean: an examination of profile data and a profile-based climatology. J. Geophys. Res. 109, C12003.

de Melo Viríssimo, F., Martin, A.P., Henson, S.A., 2022. Influence of seasonal variability in flux attenuation on global organic carbon fluxes and nutrient distributions. Glob. Biogeochem. Cycles 36 (2) p.e2021GB007101.

Fan, G., Han, Z., Ma, W., Chen, S., Chai, F., Mazloff, M.R., Pan, J., Zhang, H., 2020. Southern Ocean carbon export efficiency in relation to temperature and primary productivity. Sci. Rep. 10 (1), 1–11.

Giering, S.L., Sanders, R., Martin, A.P., Henson, S.A., Riley, J.S., Marsay, C.M., Johns, D. G., 2017. Particle flux in the oceans: challenging the steady state assumption. Glob. Biogeochem. Cycles 31 (1), 159–171.

Gomi, Y., Fukuchi, M., Taniguchi, A., 2010. Diatom assemblages at subsurface chlorophyll maximum layer in the eastern Indian sector of the Southern Ocean in summer. J. Plankton Res. 32 (7), 1039–1050.

Gordon, A.L., 1971. Oceanography of Antarctic waters. Antarctic Oceanol. I 15, 169–203.

Graff, J.R., Westberry, T.K., Milligan, A.J., Brown, M.B., Dall'Olmo, G., van Dongen-Vogels, V., Reifel, K.M., Behrenfeld, M.J., 2015. Analytical phytoplankton carbon measurements spanning diverse ecosystems. Deep-Sea Res. I Oceanogr. Res. Pap. 102, 16–25.

Graff, J.R., Westberry, T.K., Milligan, A.J., Brown, M.B., Olmo, G.D., Reifel, K.M., Behrenfeld, M.J., 2016. Photoacclimation of natural phytoplankton communities. Mar. Ecol. Prog. Ser. 542, 51–62.

Gray, A.R., Johnson, K.S., Bushinsky, S.M., Riser, S.C., Russell, J.L., Talley, L.D., Wanninkhof, R., Williams, N.L., Sarmiento, J.L., 2018. Autonomous biogeochemical floats detect significant carbon dioxide outgassing in the high-latitude Southern Ocean. Geophys. Res. Lett. 45 (17), 9049–9057.

Grigorov, I., Rigual-Hernandez, A.S., Honjo, S., Kemp, A.E., Armand, L.K., 2014. Settling fluxes of diatoms to the interior of the Antarctic circumpolar current along 170 W. Deep-Sea Res. I Oceanogr. Res. Pap. 93, 1–13.

Haëntjens, N., Boss, E., Talley, L.D., 2017. Revisiting Ocean Color algorithms for chlorophyll a and particulate organic carbon in the Southern Ocean using biogeochemical floats. J. Geophys. Res. Oceans 122 (8), 6583–6593.

Haëntjens, N., Della Penna, A., Briggs, N., Karp-Boss, L., Gaube, P., Claustre, H., Boss, E., 2020. Detecting mesopelagic organisms using biogeochemical-Argo floats. Geophys. Res. Lett. *47* (6) p.e2019GL086088.

Henson, S.A., Sanders, R., Madsen, E., 2012. Global patterns in efficiency of particulate organic carbon export and transfer to the deep ocean. Glob. Biogeochem. Cycles 26 (1).
Jin, D., Hoagland, P., Buesseler, K.O., 2020. The value of scientific research on the ocean's biological carbon pump. Sci. Total Environ. 749, 141357.
Johnson, K.S., Bif, M.B., 2021. Constraint on net primary productivity of the global ocean by Argo oxygen measurements. Nat. Geosci. 14 (10), 769–774.
Johnson, K.S., Plant, J.N., Coletti, L.J., Jannasch, H.W., Sakamoto, C.M., Riser, S.C., Swift, D.D., Williams, N.L., Boss, E., Haëntjens, N., Talley, L.D., 2017. Biogeochemical sensor performance in the SOCCOM profiling float array. J. Geophys. Res. Oceans 122 (8), 6416–6436.
Kemp, A.E., Villareal, T.A., 2018. The case of the diatoms and the muddled mandalas: time to recognize diatom adaptations to stratified waters. Prog. Oceanogr. 167, 138–149.
Kemp, A.E.S., Pearce, R.B., Grigorov, I., Rance, J., Lange, C.B., Quilty, P., Salter, I., 2006. Production of giant marine diatoms and their export at oceanic frontal zones: implications for Si and C flux from stratified oceans. Glob. Biogeochem. Cycles 20 (4).
Kienast, S.S., Torfstein, A., 2022. Evaluation of biological carbon pump metrics in the subtropical Gulf of Aqaba, Northern Red Sea. Glob. Biogeochem. Cycles 36 (10) p. e2022GB007452.
Klunder, M.B., Laan, P., Middag, R., De Baar, H.J.W., Van Ooijen, J.C., 2011. Dissolved iron in the Southern Ocean (Atlantic sector). Deep-Sea Res. II Top. Stud. Oceanogr. 58 (25–26), 2678–2694.
Kopczynska, E.E., Dehairs, F., Elskens, M., Wright, S., 2001. Phytoplankton and microzooplankton variability between the subtropical and polar fronts south of Australia: thriving under regenerative and new production in late summer. J. Geophys. Res. Oceans 106 (C12), 31597–31609.
Kwon, E.Y., Primeau, F., Sarmiento, J.L., 2009. The impact of remineralization depth on the air–sea carbon balance. Nat. Geosci. 2 (9), 630–635.
Lacour, L., Briggs, N., Claustre, H., Ardyna, M., Dall'Olmo, G., 2019. The intraseasonal dynamics of the mixed layer pump in the subpolar North Atlantic Ocean: a biogeochemical-Argo float approach. Glob. Biogeochem. Cycles 33 (3), 266–281.
Li, T., Bai, Y., He, X., Chen, X., Chen, C.T.A., Tao, B., Pan, D., Zhang, X., 2018. The relationship between poc export efficiency and primary production: opposite on the shelf and basin of the northern South China Sea. Sustainability *10* (10), 3634.
Long, J.S., Fassbender, A.J., Estapa, M.L., 2021. Depth-resolved net primary production in the Northeast Pacific Ocean: a comparison of satellite and profiling float estimates in the context of two marine heatwaves. Geophys. Res. Lett. *48* (19) p. e2021GL093462.
Maiti, K., Benitez-Nelson, C.R., Buesseler, K.O., 2010. Insights into particle formation and remineralization using the short-lived radionuclide, Thoruim-234. Geophys. Res. Lett. 37 (15).
Maritorena, S., Siegel, D.A., Peterson, A.R., 2002. Optimization of a semianalytical ocean color model for global-scale applications. Appl. Opt. 41, 2705.
Marra, J.F., Lance, V.P., Vaillancourt, R.D., Hargreaves, B.R., 2014. Resolving the ocean's euphotic zone. Deep-Sea Res. I Oceanogr. Res. Pap. 83, 45–50.
Maurer, T.L., Plant, J.N., Johnson, K.S., 2021. Delayed-mode quality control of oxygen, nitrate, and ph data on SOCCOM biogeochemical profiling floats. Front. Mar. Sci. 1118.
Myriokefalitakis, S., Ito, A., Kanakidou, M., Nenes, A., Krol, M.C., Mahowald, N.M., Scanza, R.A., Hamilton, D.S., Johnson, M.S., Meskhidze, N., Kok, J.F., 2018. Reviews and syntheses: the GESAMP atmospheric iron deposition model intercomparison study. Biogeosciences 15 (21), 6659–6684.
Organelli, E., Dall'Olmo, G., Brewin, R.J., Tarran, G.A., Boss, E., Bricaud, A., 2018. The open-ocean missing backscattering is in the structural complexity of particles. Nat. Commun. 9 (1), 5439.
Orsi, A.H., Whitworth III, T., Nowlin Jr., W.D., 1995. On the meridional extent and fronts of the Antarctic Circumpolar Current. Deep-Sea Res. I Oceanogr. Res. Pap. 42 (5), 641–673.
Owens, S.A., Pike, S., Buesseler, K.O., 2015. Thorium-234 as a tracer of particle dynamics and upper ocean export in the Atlantic Ocean. Deep-Sea Res. II Top. Stud. Oceanogr. 116, 42–59.
Parslow, J.S., Boyd, P.W., Rintoul, S.R., Griffiths, F.B., 2001. A persistent subsurface chlorophyll maximum in the Interpolar frontal zone south of Australia: seasonal progression and implications for phytoplankton-light-nutrient interactions. J. Geophys. Res. Oceans 106 (C12), 31543–31557.
Queguiner, B., 2013. Iron fertilization and the structure of planktonic communities in high nutrient regions of the Southern Ocean. Deep-Sea Res. II Top. Stud. Oceanogr. 90, 43–54.
Rembauville, M., Briggs, N., Ardyna, M., Uitz, J., Catala, P., Penkerc'h, C., Poteau, A., Claustre, H., Blain, S., 2017. Plankton assemblage estimated with BGC-Argo floats in the Southern Ocean: implications for seasonal successions and particle export. J. Geophys. Res. Oceans 122 (10), 8278–8292.
Roesler, C., Uitz, J., Claustre, H., Boss, E., Xing, X., Organelli, E., Briggs, N., Bricaud, A., Schmechtig, C., Poteau, A., d'Ortenzio, F., 2017. Recommendations for obtaining unbiased chlorophyll estimates from in situ chlorophyll fluorometers: a global analysis of WET labs ECO sensors. Limnol. Oceanogr. Methods 15 (6), 572–585.
Schrader, P.S., Milligan, A.J., Behrenfeld, M.J., 2011. Surplus photosynthetic antennae complexes underlie diagnostics of iron limitation in a cyanobacterium. PLoS One *6* (4) p.e18753.
Siegel, D.A., Buesseler, K.O., Doney, S.C., Sailley, S.F., Behrenfeld, M.J., Boyd, P.W., 2014. Global assessment of ocean carbon export by combining satellite observations and food-web models. Glob. Biogeochem. Cycles 28 (3), 181–196.
Sournia, A., 1982. Form and function in marine phytoplankton. Biol. Rev. 57 (3), 347–394.
Sullivan, J.M., Twardowski, M.S., Ronald, J., Zaneveld, V., Moore, C.C., 2013. Measuring optical backscattering in water. In: Light Scattering Reviews, 7. Springer, Berlin, Heidelberg, pp. 189–224.
Szabó, E., Kulin, A., Korányi, L., Literáti-Nagy, B., Cserepes, J., Somogyi, A., Sarkadi, B., Várady, G., 2021. Alterations in erythrocyte membrane transporter expression levels in type 2 diabetic patients. Sci. Rep. 11 (1), 1–10.
Thode, H.C., 2002. Plots, probability plots and regression tests. In: Testing for Normality, 164. CRC Press. https://doi.org/10.1201/9780203910894.
Uchida, T., Balwada, D., Abernathey, R., Prend, C.J., Boss, E., Gille, S.T., 2019. Southern Ocean phytoplankton blooms observed by biogeochemical floats. J. Geophys. Res. Oceans 124 (11), 7328–7343.
Wyatt, N.J., Milne, A., Woodward, E.M.S., Rees, A.P., Browning, T.J., Bouman, H.A., Worsfold, P.J., Lohan, M.C., 2014. Biogeochemical cycling of dissolved zinc along the GEOTRACES South Atlantic transect GA10 at 40 S. Glob. Biogeochem. Cycles 28 (1), 44–56.
Xing, X., Claustre, H., Blain, S., D'Ortenzio, F., Antoine, D., Ras, J., Guinet, C., 2012. Quenching correction for in vivo chlorophyll fluorescence acquired by autonomous platforms: a case study with instrumented elephant seals in the Kerguelen region (Southern Ocean). Limnoogy Oceanogr. Methods 1, 483–495.